


Equiaxed Polycrystalline Ice for Ultrasonic Testing of Solids

Francesco Simonetti^{1,*} and Michael D. Uchic^{2,†}

¹*Department of Aerospace Engineering and Engineering Mechanics, University of Cincinnati, Cincinnati, Ohio 45221, USA*

²*Air Force Research Laboratory, Materials and Manufacturing Directorate, Wright-Patterson AFB, Ohio 45433, USA*

 (Received 6 January 2022; revised 24 May 2022; accepted 25 May 2022; published 14 July 2022)

Elastic waves traveling through polycrystalline ice Ih can experience distortion due to the transversely isotropic structure of its crystals. This can pose a challenge to nondestructive ultrasonic testing when ice is used as a coupling medium to transfer energy between an ultrasonic source and the solid to be inspected for the presence of damage. Here, it is shown that when ice is grown on a metallic solid using directional freezing techniques, it develops a coarse columnar grain structure, which causes the ultrasonic signals to vary greatly depending on which region of the ice volume is interrogated. On the other hand, if small ice particles are compacted around the solid and saturated with degassed liquid water before directional freezing, an equiaxed grain structure is obtained, which behaves as a homogeneous and isotropic medium. Furthermore, it is demonstrated that ultrasonic transmission through an ice-metal interface can be achieved regardless of the angle formed between the ultrasonic beam and the interface. Therefore, it is possible to overcome one of the fundamental limitations of conventional water coupling, which prevents transmission when the beam is not close to orthogonal to the interface due to the total reflection phenomenon. This property is useful to expand the scope of the application of ultrasonic testing to solids with complex geometries such as those obtained with additive manufacturing methods.

DOI: [10.1103/PhysRevApplied.18.014034](https://doi.org/10.1103/PhysRevApplied.18.014034)

I. INTRODUCTION

To ensure the safe and cost-effective operation of complex machines, their critical components must be tested with nondestructive evaluation (NDE) methods to detect the presence of flaws, which, if left unchecked, may grow to a critical size and cause structural failure. NDE methods that utilize elastic waves in the ultrasonic regime are widely used across many industries thanks to their ability to penetrate inside materials at depths greater than those possible with other forms of radiation, e.g., x rays, and their high sensitivity to a wide spectrum of defects, including voids and cracks [1–3].

Testing is commonly performed by immersing a component in water, which allows energy to be transferred from an ultrasonic transducer to the component and *vice versa* [4]. However, in the presence of metallic components, the energy that can be transmitted through a water-metal interface is relatively low and it may even vanish when the ultrasonic beam is not close to orthogonal to the interface. Since achieving sufficient energy transmission is essential to probe the interior of a solid, ultrasonic testing is

currently limited to the so-called *sonic* shapes, which are characterized by rectilinear contours that can be maintained normal to the ultrasonic beam.

Recent progress in near-net shape manufacturing technologies, such as metal additive manufacturing [5], is driving the need for the inspection of components that may have curved boundaries and present internal features such as vanes and channels. Therefore, there is an urgent need to advance the state of the art in ultrasonic testing beyond the inspection of simple sonic shapes [6–8].

To address the limitations of immersion ultrasonic testing, one possibility is to freeze the water and take advantage of the remarkable physicochemical properties of ice, notably its high speed of sound [9] (approximately 4000 m s^{-1} versus 1500 m s^{-1} in water). Currently, 13 crystalline and several amorphous phases of ice have been identified depending on which temperature and pressure intervals of the water phase diagram are considered [10,11]. At temperatures above -200°C and pressures below 200 MPa, ice exhibits hexagonal symmetry and is known as ice Ih, this being the crystalline structure predominant on Earth and the one of interest in ultrasonic testing.

The rationale for the practicality of ultrasonic testing with ice coupling in NDE has been articulated in a

*f.simonetti@uc.edu

†michael.uchic@us.af.mil

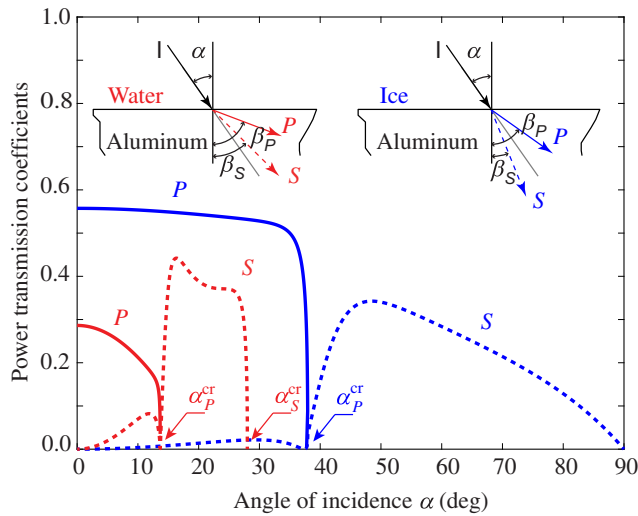


FIG. 1. Ultrasonic power transmission into an aluminum half space through water (red) and ice (blue) coupling. The incident field is a compressional (P) wave whose propagation direction forms an angle α with the normal to the aluminum surface. The transmitted wave field consists of a plane P wave (solid curve) refracted at angle β_P and a mode converted shear (S) wave (dashed curve) propagating at angle β_S . The angles $\alpha_{P,S}^{cr}$ mark the critical incidences beyond which the transmitted wave mode becomes evanescent. With ice coupling transmission is possible at all angles while, with water, power cannot be transmitted beyond $\alpha_S^{cr} = 28^\circ$.

few recent papers [12–14]. Here, instead the focus is on presenting the physical aspects that underpin the case for ice coupling. For this purpose, Fig. 1 considers a water-aluminum and an ice-aluminum planar interface, each subject to an incident plane wave. The power transmitted through an interface is given as a function of the angle, α , formed between the incident wave and the normal to the interface. In both cases, the incident wave is a compressional wave (P wave) and the transmitted power is carried by a P wave and a mode-converted shear wave (S wave). The curves are obtained using the standard elastodynamic theory of plane-wave scattering by interfaces [15] assuming that all the media are isotropic and homogeneous (material properties are listed in Table I) and that the media are perfectly bonded at the interface to ensure continuity of displacement and stress.

When a wave of power, I , impinges on the interface at normal incidence ($\alpha = 0$), no mode conversion occurs and the power coefficient of the transmitted P wave, is $I_T/I = 4\Phi/(\Phi + 1)^2$ where I_T is the power of the transmitted wave and Φ is the ratio between the acoustic impedances, Z , of the two media. For each medium, Z is defined as the product between mass density, ρ , and compressional wave speed, c_P , i.e., $Z = \rho \times c_P$. The larger the impedance contrast between media, the further the impedance ratio Φ is from unity and therefore the lower the transmission

TABLE I. Ultrasonic velocities and densities of the materials used in this study. The velocities are obtained from standard travel-time measurements, which, for the metals, are conducted at room temperature. For ice, the data is measured from equiaxed polycrystalline specimens.

Materials	P -wave velocity (m s ⁻¹)	S -wave velocity (m s ⁻¹)	Density (kg m ⁻³)
Water	1480		1000
Ice Ih (−10 °C)	3850	1850	918
Aluminum 7075	6260	3150	2810
Titanium Ti-6Al-4V	6106	3060	4430
Brass	4492	1790	9074
Inconel 718	5695	3030	8220

coefficient. For typical metallic alloys used in engineering applications, only 10–30% of the power is transmissible through a single water-metal interface while the power almost doubles when considering ice-metal interfaces [12]. Under oblique incidence, the transmitted P and S waves are refracted at angles β_P and β_S satisfying Snell's law, i.e., $\sin \beta_P = (c_P^m/a) \sin \alpha$ and $\sin \beta_S = (c_S^m/a) \sin \alpha$ where a is the speed of sound of P waves in the coupling medium (water or ice) and c_P^m and c_S^m are the velocities of P and S waves in the second medium, respectively. As α increases, the power of the transmitted P wave decreases until α reaches a critical value, α_P^{cr} , that depends only on velocities a and c_P^m , i.e., $\alpha_P^{cr} = \arcsin(a/c_P^m)$. With water coupling, $\alpha_P^{cr} \approx 10 - 15^\circ$ for most metals while this value increases to about 40° under ice coupling. Beyond α_P^{cr} , the transmitted P wave becomes evanescent and energy is only carried by the mode converted S wave until a second shear critical angle $\alpha_S^{cr} = \arcsin(a/c_S^m)$ is reached. For greater angles of incidence, transmission is no longer possible and therefore internal flaws are not detectable. However, the second critical angle exists only if the speed of P waves in the coupling medium is lower than c_S^m . Under water coupling, α_S^{cr} is typically below 30° . On the other hand, no shear critical angle occurs at ice-metal interfaces since the shear velocity of metals is typically well below 3500 m s^{-1} while the velocity of P waves in ice approaches 4000 m s^{-1} .

Based on the above observations, ice coupling is advantageous over immersion because (a) it overcomes the fundamental physical limitation imposed by the existence of α_S^{cr} in immersion; (b) the transmission coefficient does not experience the same rapid decrease observed as α approaches α_P^{cr} with water coupling; (c) the transmitted power is substantially higher even for low angles of incidence; (d) beam refraction diminishes and becomes negligible after α_P^{cr} for those metallic alloys, which have a ratio c_S^m/a approaching unity.

The analysis of Fig. 1 is based on the fundamental assumptions that ice is a homogenous and isotropic material and that it is perfectly bonded to the metallic substrate.

The latter is generally true owing to ice excellent adhesion properties to hydrophilic surfaces [16–18] or surfaces with some degree of roughness [19,20] and has been confirmed by ultrasonic experiments at frequencies as high as 15 MHz [13]. Additionally, while with other materials the liquid-to-solid phase transition is accompanied by a volume contraction, water expands as it solidifies, which further prevents the possibility of debonding at the ice-metal interfaces.

On the other hand, the conditions under which ice can be produced to meet the homogeneity and isotropy requirements are less apparent. Current efforts to control the structure of ice have been limited to avoid the formation of porosity (air bubbles) and cracks by combining directional freezing and water stirring [13]. For this purpose, the component is placed in a plastic container with a metallic base. The container is filled with water, which is then cooled from the base. This generates a quasiplanar freeze front that advances vertically, bottom to top, until the component is fully encapsulated in a block of crystal clear ice. Throughout the freezing process, continuous water flow is maintained above the freeze front to avoid that air dissolved in water may reach supercritical concentration and lead to the nucleation of bubbles that may then be engulfed by the front [21,22]. Moreover, since water is always free to expand, ice forms under constant pressure conditions, which prevent the build up of internal stresses, thus avoiding the formation of fractures and cracks. This also excludes the possibility that ice may damage the component [13].

While the current method is effective in preventing the formation of pores and cracks, the polycrystalline structure of ice could still be a significant source of heterogeneity and anisotropy. In fact, the hexagonal structure of ice Ih means that an ice single crystal exhibits transverse isotropy. As a result, the speed of elastic waves is dependent on the angle, θ , formed between the crystallographic axis (c axis) and the wave propagation direction. Tamura *et al.* [23] predicted that at -2°C the velocity of quasi- P -waves decreases from 3875 m s^{-1} to 3600 m s^{-1} as θ increases from 0° to 45° and subsequently increases to 3760 m s^{-1} as θ increases to 90° .

If the crystals are equiaxed and randomly oriented, the propagation of ultrasonic waves in the polycrystalline material can be described in terms of an effective medium that is homogeneous and isotropic [24]. In particular, the wave field is decomposed into a coherent field, whose propagation is determined by the effective medium properties, and an incoherent component, which depends on the properties of each of the grains encountered by the wave field [25]. Ideally, the coherent component should be dominant in polycrystalline ice. The relative strength of the two components is governed by elastic scattering effects at the grain boundaries, which also cause attenuation, ζ , of the coherent field with propagation distance.

Consequently, the mean grain size, δ , and the wavelength, Λ , are the parameters, which, together with the degree of anisotropy of the grains, determine the attenuation level and ultimately if equiaxed polycrystalline ice can achieve the desired homogeneity and isotropy properties.

A vast body of work exists on unified models to relate the effective medium properties, including ζ , to δ and Λ starting from pioneering studies in the 1980s [25–27] to more recent contributions accounting for more complex grain structures [28–31] including texture in polycrystalline ice [32]. Here, it is sufficient to observe that to limit the incoherent field one must operate in the Rayleigh ($\delta < \Lambda$) or, to a certain extent, in the stochastic ($\delta \sim \Lambda$) scattering regimes while avoiding the geometrical regime ($\delta > \Lambda$) where the coherent field becomes weak and is dominated by the incoherent component.

The grain structure of the ice produced by the current encapsulation methods has not been investigated. However, microscopy studies by Camp [33] and more recently Pach *et al.* [34] have shown that ice directly grown on a metallic substrate exhibits a columnar grain structure, which, in contrast with the directional growth of columnar ice on a lake surface [35], shows no preferential orientation of the c axes. This suggests that a similar columnar growth may occur when directional freezing is used to embed a solid in ice. Notably, in the field of glaciology, the microstructure of ice test cylinders is controlled by applying directional freezing to an ice-particle compact saturated with degassed water rather than pure water [36,37]. This leads to polycrystalline specimens with fine equiaxed grain structure whose grain size is controlled by selecting the initial size of the ice particles.

This paper aims at investigating the effect that different ice-grain structures have on the propagation of ultrasonic waves. The main objective is to show that with equiaxed ice it is possible to overcome the limitations of immersion ultrasonic testing and achieve transmission into a broad range of metals regardless of the angle of incidence of the ultrasonic beam, thus confirming the predictions from Fig. 1.

The paper begins with a description of the experimental and numerical methods in Sec. II, which is followed by results in Sec. III. In Sec. IV the applicability of ice coupling in practical nondestructive testing is discussed. Finally, concluding remarks are presented in Sec. V. The methods in Sec. II include encapsulation techniques (Sec. II A); ultrasonic measurements (Sec. II B); visualization of grain structure (Sec. II C); and elastic full-wave simulations (Sec. II D). The results are presented in two parts: Sec. III A considers the effect of different grain structures and ultrasonic wavelengths while Sec. III B analyzes oblique incidence and compares experiments to simulations. A comparison with immersion testing is also provided in Sec. III B.

II. METHODS

A. Specimen preparation

Each specimen consists of an ice block containing two rectangular plates made of one of the metals listed in Table I. The specimens are prepared by first placing the two plates in a 177.8-mm diameter cylindrical acrylic mold with an aluminum base as shown in Fig. 2(a). The plates have the dimensions indicated in Fig. 2(b) and contain a 2-mm diameter, 30-mm length, side-drilled hole (SDH) that is used as an internal reflector during the ultrasonic tests. The SDH is connected to two, 5.1-mm diameter, threaded holes each used to mount a pivot that allows the plates to be held in position by a frame attached to the base of the mold, Fig. 2(a). To prevent the ingress of water inside the SDH, its ends are sealed with silicone before

mounting the pivots. Set screws acting on the pivots are used to secure the position of the plates so as to maintain one plate parallel to the base of the mold (reference plate) while the other is slanted at the desired angle of incidence.

Two ice encapsulation methods are employed, here referred to as the water-stirring method (WSM) and the ice-particle compact method (IPCM). Both use the directional freezer described in Ref. [13], which forces the heat flow through the base of the mold only. However, the two methods differ in that with WSM the mold containing the plate assembly is filled with water while with IPCM ice powder is compacted into the mold, which is then saturated with degassed water. Details of WSM are given in Ref. [13], whereas the procedure for IPCM has been described in Ref. [36,37]. In this study, the ice powders are produced by crushing blocks of clear ice in a kitchen blender and then sieving the grains (600- μm mesh) at -20°C in a chest freezer to remove larger particles. The powders are subsequently compacted into the mold (with the plate assembly) to achieve a porosity of approximately 50%. At the end of the freezing process, the top surface of the ice block is partially melted with a warm plate to obtain a flat and smooth surface parallel to the base of the mold and hence to the reference plate.

B. Ultrasonic testing and signal processing

Ultrasonic raster scans of the ice specimens are performed at -10°C using a computer-controlled motion system housed in a freezer as described in Ref. [13]. A spring-loaded probe holder is used to maintain a single-element, *P*-wave transducer in contact with the surface of the ice block during the scans as shown in Fig. 3(a). Thanks to the mirrorlike finish of the ice-block surface, a few droplets of liquid couplant are sufficient to perform an entire scan. Here, the couplant is a water-glycol mixture that remains in the liquid phase at -10°C .

The transducer is operated in pulse-echo mode through a pulser receiver that feeds a voltage spike into the transducer and subsequently preamplifies the signal received by the transducer before sending it to an oscilloscope for visualization and digital data capture. Figure 3(b) shows a typical waveform measured with a 3.5-MHz center frequency, 12.7-mm (1/2") diameter transducer for a scan point above the reference plate. The signal consists of a train of pulses with the first one corresponding to the reflection from the top ice-aluminum interface, this being referred to as the front-surface (FS) reflection. The pulses trailing the FS reflection result from the transmission of energy inside the plate and its subsequent reverberation within the plate thickness.

The waveforms are used to generate *B* scans and *C* scans. *B* scans are formed from the waveforms measured

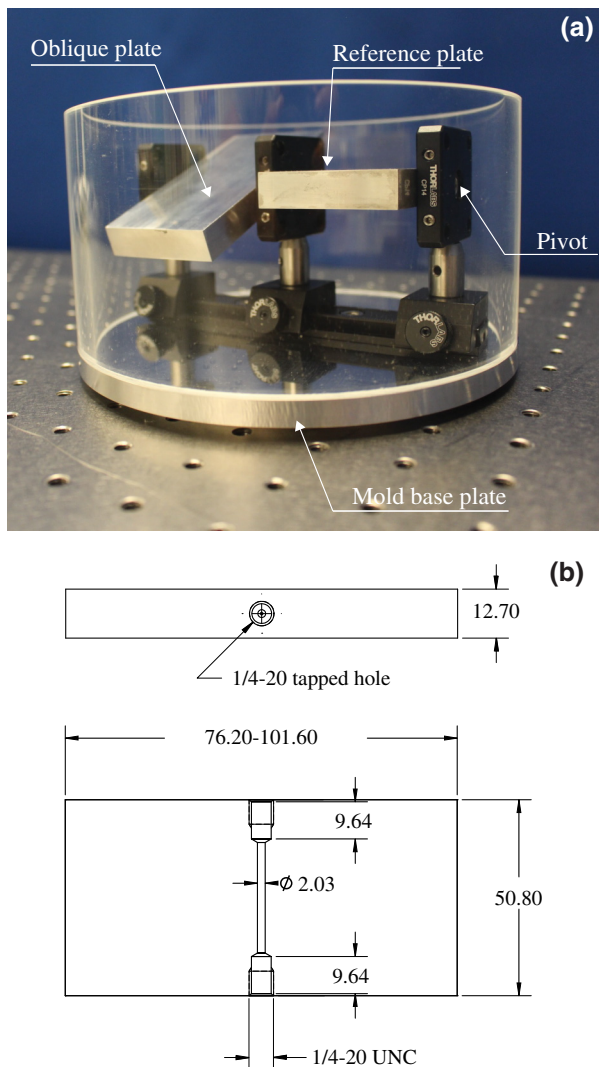


FIG. 2. Specimen configuration for freezing experiments. (a) Mold and plate assembly; (b) Plate geometry.

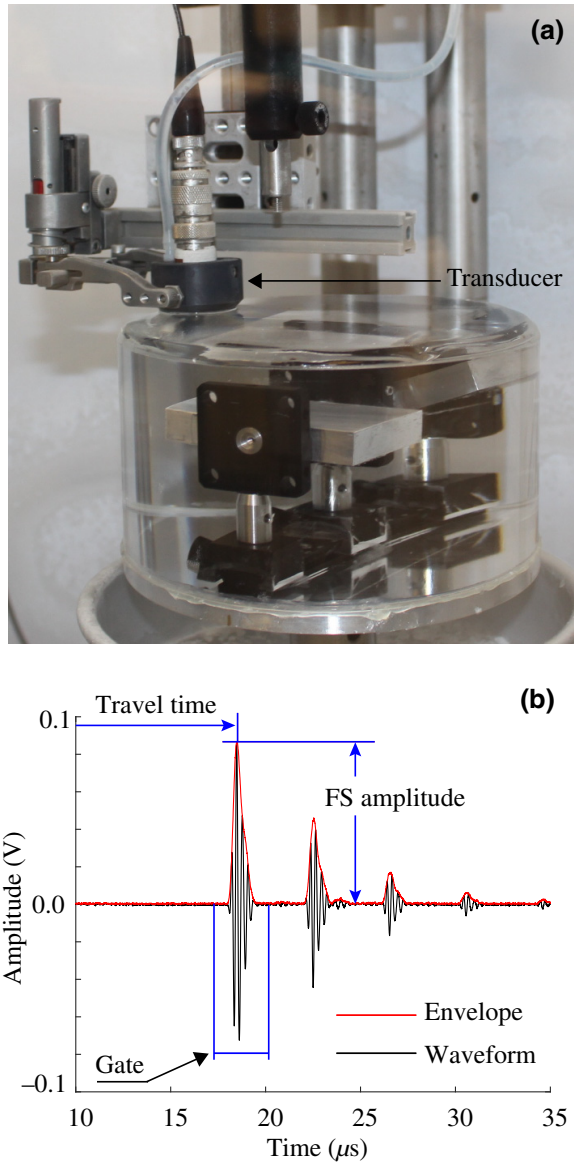


FIG. 3. (a) Example of the ice block obtained with the water-stirring method, showing the internal reference and slanted plates; (b) pulse-echo signal measured above the reference plate with a 3.5-MHz transducer.

along a single line scan and show the amplitude of the signal as a function of time and position. A *C* scan targets selected features of the signals over prescribed time intervals referred to as gates. For instance, in Fig. 3(b) the gate is set to capture the FS reflection. A gate fully comprised between the first two pulses, would target the reflection from the SDH. The features of interest considered here are the maximum amplitude of the signal envelope within the gate and the time at which it occurs, referred to as the travel time. A *C* scan is therefore a map showing either amplitude or travel time as a function of position in the raster scan.

C. Grain characterization

The grain structure of the ice specimens is visualized by exploiting the optical birefringence of hexagonal ice crystals. Ice samples are cut into slices approximately 2-mm thickness using a band saw. The thickness is then reduced to about 250 μm by placing the slices on a warm plate. Images of the grain structure are captured with a digital camera after placing the slices between the cross-polarizing filters of a polariscope. The images are processed with the linear intercept length method to determine the grain-size distribution [38].

D. Numerical simulations

The ultrasonic experiments are simulated using the finite difference method, which achieves high numerical efficiency when modeling wave propagation in highly heterogeneous media and is indeed one of the most popular methods used in seismic wave studies [39]. This is particularly relevant to ice-encapsulated components since the medium formed by ice and the component exhibits a significant level of heterogeneity due to the contrast between the mechanical properties of ice and those of metals. Here, an in-house C++ code based on the explicit finite-difference time-domain (FDTD) scheme is used. The scheme employs the two-dimensional (2D) velocity-stress formulation of the elastodynamic equations in the *x-z* plane. The equations are cast in terms of the normal stress components σ_x and σ_z , the shear stress τ_{xz} , and the particle velocity components v_x and v_z , i.e.,

$$\rho \frac{\partial v_x}{\partial t} = \frac{\partial \sigma_x}{\partial x} + \frac{\partial \tau_{xz}}{\partial z}, \quad (1)$$

$$\rho \frac{\partial v_z}{\partial t} = \frac{\partial \tau_{xz}}{\partial x} + \frac{\partial \sigma_z}{\partial z}, \quad (2)$$

$$\frac{\partial \sigma_x}{\partial t} = (\lambda + 2\mu) \frac{\partial v_x}{\partial x} + \lambda \frac{\partial v_z}{\partial z}, \quad (3)$$

$$\frac{\partial \sigma_z}{\partial t} = (\lambda + 2\mu) \frac{\partial v_z}{\partial z} + \lambda \frac{\partial v_x}{\partial x}, \quad (4)$$

$$\frac{\partial \tau_{xz}}{\partial t} = \mu \left(\frac{\partial v_x}{\partial z} + \frac{\partial v_z}{\partial x} \right), \quad (5)$$

where t is time and λ and μ are the Lamé constants, which are related to the speed of *P* and *S* waves, i.e.,

$$c_P = \sqrt{\frac{\lambda + 2\mu}{\rho}}, \quad c_S = \sqrt{\frac{\mu}{\rho}}. \quad (6)$$

The above equations allow for material heterogeneities since λ , μ , and ρ can be functions of position. However, they are underpinned by an elastic and isotropic constitutive model between stress and strain and therefore do not account for ultrasonic anisotropy and material damping.

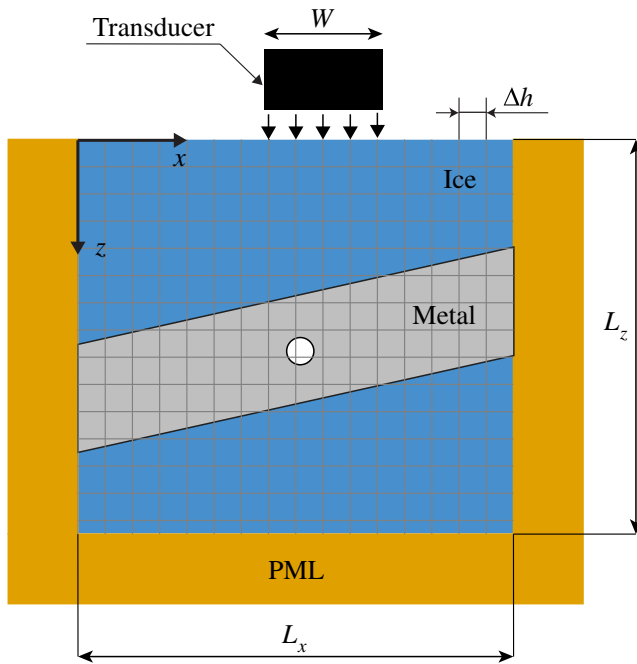


FIG. 4. Two-dimensional finite-difference model for the simulation of ultrasonic wave propagation through an ice block containing a metal plate. Perfectly matched layers (PMLs) are used to suppress reflections from the boundaries of the domain with the exception of the top surface where the traction-free boundary condition is enforced. The transducer excitation is modeled by applying normal stress at the nodes below the aperture W of the transducer.

The FDTD scheme solves the finite-difference equations obtained by introducing a staggered grid in space and time according to the method proposed by Virieux [40]. A square grid of size Δh is generated over a rectangular domain ($L_x \times L_z$) consisting of ice and metal regions as shown in Fig. 4. To account for sharp discontinuities in material properties at the ice-metal interfaces, the values of buoyancy (reciprocal of density) and μ at the staggered nodes are computed as the arithmetic and harmonic averages of the corresponding values at the neighboring nodes [41]. The condition to achieve numerical stability is

$$\Delta t < \frac{\Delta h}{c_P \sqrt{2}}, \quad (7)$$

where Δt is the time step and c_P is the largest speed in the domain.

The sides and bottom of the domain are connected to perfectly matched layers (PMLs) that absorb the waves that reach the boundaries of the domain and suppress the reflections that would otherwise be produced by these artificial boundaries. Here, the split PML formulation described by Collino and Tsogka [42] is used based on a

damping function, $d(s)$, defined as

$$d(s) = -\frac{3c_P \ln Q}{2\Delta} \left(\frac{s}{\Delta}\right)^2, \quad (8)$$

where Δ is the thickness of the absorbing layer and s is the minimum distance between a point inside the layer and the interface between the layer and domain. Q is a coefficient that is typically in the range 10^{-3} – 10^{-6} . Since the same grid size as the main domain is used inside the layers, the values of Δ and Q are selected by trial and error to minimize the unwanted reflections while limiting computation time.

The traction-free boundary condition at the top of the domain is implemented using the image-stress method [43]. However, to model the transducer excitation, a uniform pressure, P , is applied at the nodes beneath the width, W , of the transducer. The temporal dependence of P is modeled as a Hann windowed wave pulse. The pulse-echo response from the transducer is obtained by integrating the surface values of v_z over the length W .

In the simulations presented in this paper, P is modeled as a four-cycle, 3.5-MHz center frequency pulse. To achieve high accuracy, the element size, Δh , is set to $20 \mu\text{m}$, which corresponds to $1/25$ of the wavelength of shear waves in ice (the shortest of all wavelengths). This results in a typical model size of over 10 million nodes. A time step of 1.7 ns is used to guarantee numerical stability. Moreover, it is found that for the PMLs to be effective it is sufficient to set Δ equal to the largest wavelength and the Q value to 10^{-4} .

The material properties of the ice and metal regions are obtained by converting the ultrasonic velocities in Table I to Lamé constants using the expressions in Eq. (6). Moreover, the SDH is modeled as an air inclusion. This is sufficiently accurate for the scope of this paper and avoids the need for imposing the traction-free condition on a curved boundary that is notoriously difficult with finite-difference schemes [44].

III. RESULTS

A. Columnar versus equiaxed grain structure

With WSM the progression of directional freezing is mediated by the propagation of a freeze front that separates the solid and liquid phases of water. In a mold that contains only water the front remains planar throughout the solidification process. However, when it encounters a thermally conductive obstacle, the front bends to align with the most favorable thermal gradients through the obstacle. An example is given in Fig. 5, which shows the front (pointed by the arrows) at the beginning of the freezing process. Since ice is a poor thermal conductor, the metal frame used to hold the plates provides a path of least resistance for heat, which promotes ice growth outside the plane of the

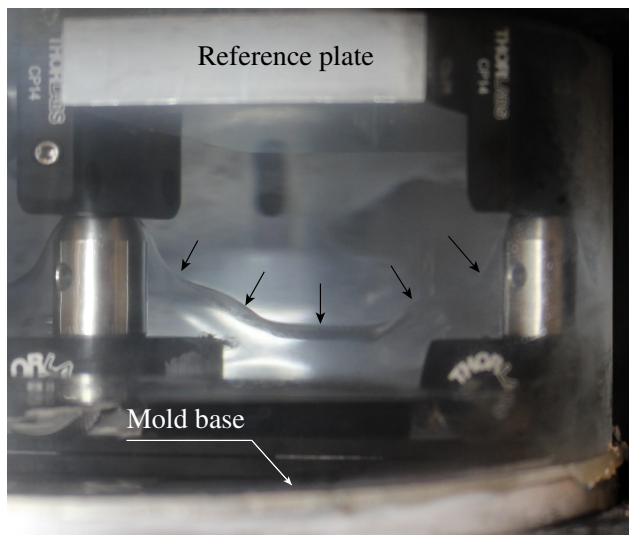


FIG. 5. Shape of the freeze front formed during the initial stages of the solidification process with the water-stirring method. The arrows indicate the outline of the front above which is liquid water.

initial front and therefore causes its deformation. Once the front reaches the plate, the same mechanism takes place. First, a thin ice film that is connected to the front rapidly spreads over the surface of the plate. The outline of the film becomes the new front, which then continues to propagate outward from the plate.

Figure 6 (left) shows the structure of the ice volume produced above the reference plate with WSM. The section

orthogonal to the plate exhibits a clear columnar grain structure with the larger dimension of the grains oriented orthogonal to the plate. Moreover, the visibility of grains in the ice section parallel to the surface of the plate, demonstrates that the c axes of the crystals are randomly oriented and are not all orthogonal to the plate. In fact, if this were the case the grains would all appear black as no birefringence would occur when the incident light is orthogonal to the ice slice (parallel to the c axes). It is worthwhile to observe that the grain width is typically in the order of several millimeters and is characterized by a broad distribution. In some specimens grains as wide as 30 mm are observed.

When the experiment is repeated with IPCM, the solidification process continues to be mediated by the propagation of a freeze front. As the front travels through the water-saturated ice particles, the particles grow until the interstitial spaces between them are filled, thus limiting overall grain size and blocking preferential growth in the direction of the heat flow. The final grain size is therefore determined by the initial size of the ice particles and their volume fraction. Moreover, since the c axes of the particles are randomly oriented, the resulting grain structure is also randomly oriented. This is demonstrated in Fig. 6 (right), which again shows sections of the ice volume above the reference plate. IPCM achieves equiaxed grain structure with 0.7-mm mean grain size and 3.6-mm standard deviation.

The specimens obtained with IPCM show lower optical clarity than those produced with WSM as it can be observed from the comparison of Fig. 7 with Fig. 3. This is

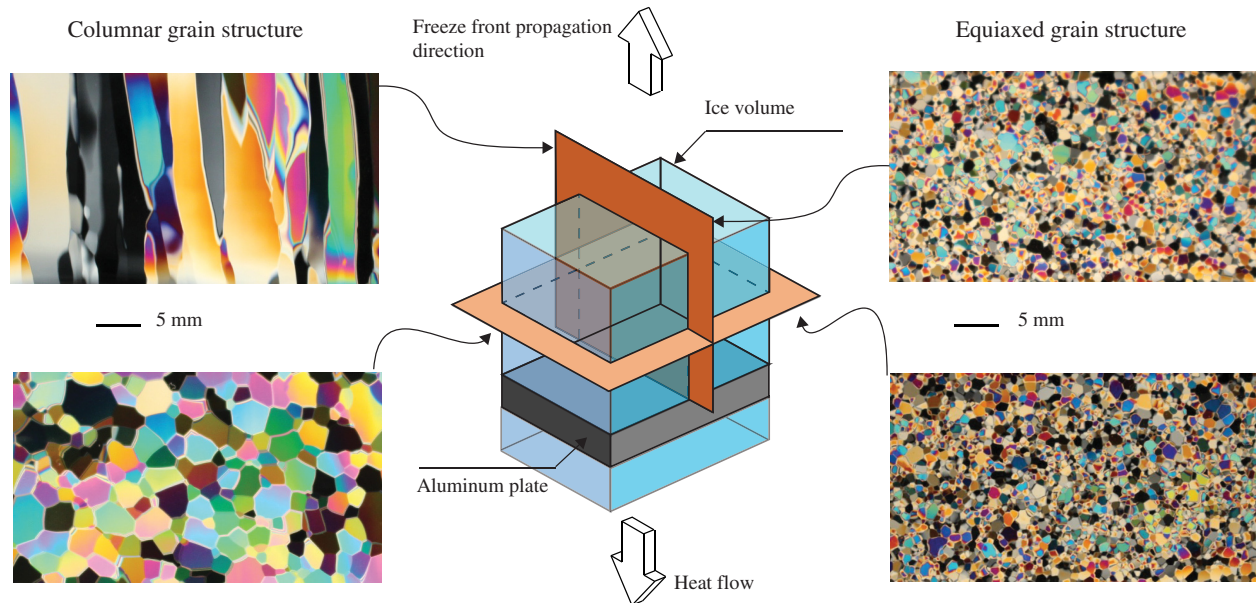


FIG. 6. Cross-polarized light images of the grain structure of ice grown on an aluminum plate under directional freezing. The columnar structure is obtained with the water-stirring method, while the equiaxed structure is produced with the ice-particle compact method. The images show typical structures observed when thin ice slices are cut parallel or orthogonal to the plate.

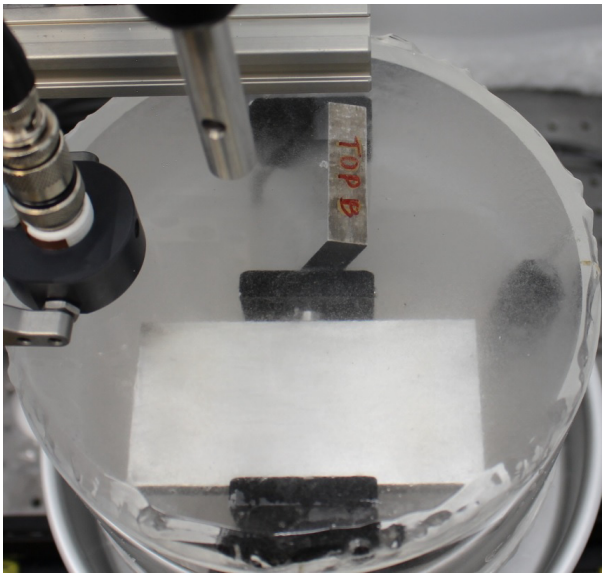


FIG. 7. Reduced ice clarity is observed in the specimen made with the ice-particle compact method compared to the specimen obtained with the water-stirring method in Fig. 3(a). This is caused by residual porosity between the ice grains.

due to microbubbles that remain primarily trapped between the ice grains and cause material porosity. The level of porosity depends on the extent to which air can be removed from the water-saturated ice compact. For this reason, it is necessary to use degassed water and perform the water-saturation process under vacuum [36]. Therefore, it is possible that the porosity level may be reduced by performing the water-saturation step at lower pressure than that possible with the current setup (10 Torr).

A practical advantage of IPCM over WSM is that the time to freeze the water-saturated ice particles, t_c , is substantially less than the time required to freeze the same volume of pure water, t_w . In fact, following the reasoning in Ref. [13] it is easily shown that $t_c = (1 - \phi)t_w$, where ϕ is the volume fraction of the ice particles. In the experiments reported in this study, where $\phi = 0.5$, the freezing time is halved.

The effect that the grain structure has on the ultrasonic wave propagation is illustrated in Fig. 8, which shows C scans of the FS reflection over the aluminum reference plate in the case of columnar, Fig. 8(a), and equiaxed grains, Fig. 8(b). For each case, the scans are measured with 3.5-MHz (12.7 mm diameter) and 5-MHz (6.35 mm diameter) transducers.

At 3.5 MHz, the columnar grain structure leads to large fluctuations in both amplitude and travel time. This is the result of the ultrasonic signals traveling primarily along the length of the columnar grains. Since the c axis of each grain is randomly oriented, the speed of the ultrasonic signal changes randomly between neighboring grains due to the

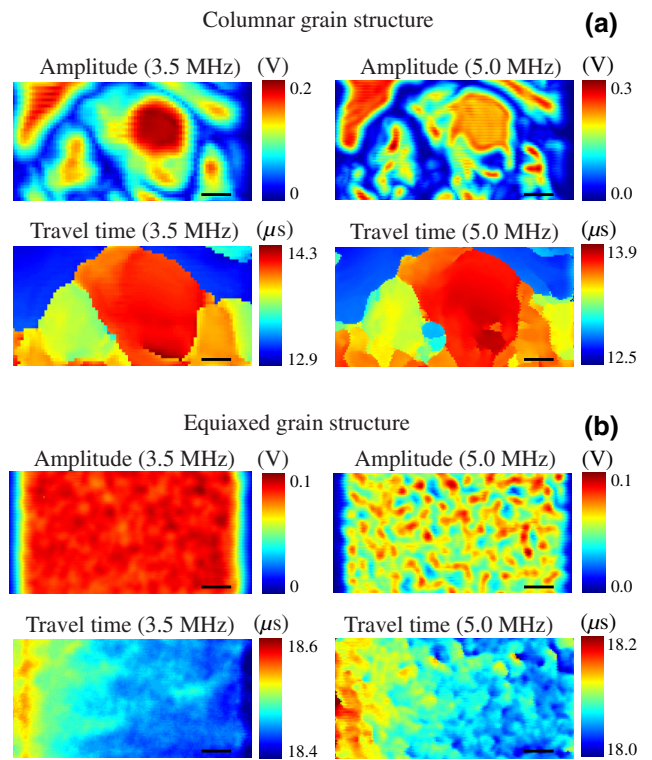


FIG. 8. Amplitude and travel-time maps (C scans) of the front-surface reflection from the reference aluminum plate measured with 3.5-MHz (12.7 mm diameter) and 5-MHz (6.35 mm diameter) transducers. (a) Columnar grain structure; (b) equiaxed structure. The scale bar is 10 mm.

anisotropy of the ice crystals. When the transducer insonifies a single large grain, the detected amplitude is large due to the very low ultrasonic attenuation in ice single crystals [23,45]. On the other hand, if the beam intersects multiple grains, each grain transfers part of the ultrasonic energy from the transducer to the FS and then back to the transducer. Since the travel time is different between grains, destructive interference may occur when the energy is recombined at the transducer thus leading to lower amplitude. Additional amplitude losses are caused by refraction occurring along those grain boundaries that are not strictly normal to the plate and cause energy to be deviated off from the main beam. When the scans are repeated at 5 MHz, the same features are observed in the amplitude and travel-time maps. The narrower ultrasonic beam now leads to higher spatial resolution, which begins to reveal the boundaries between individual grains.

The scans with the equiaxed grain structure show very different features. Despite the larger thickness of the equiaxed ice layer (36 mm versus 26 mm of the columnar grain specimen), the amplitude and travel-time C scans at 3.5 MHz are substantially more uniform, Fig. 8(b). Note that the range of travel-time variations is less than 15% of that observed with columnar ice and is primarily due to

artifacts caused by the edges of the plate and a small misalignment between the FS of the aluminum reference plate and the top surface of the ice block that causes a travel-time gradient with transducer position.

The uniformity of the maps indicates that at 3.5 MHz equiaxed polycrystalline ice can be represented by an effective medium that is homogeneous. From travel-time measurements, the effective velocities at -10°C are estimated to be 3850 m s^{-1} and to be 1850 m s^{-1} for P waves and S waves, respectively. The P -wave attenuation is currently estimated to be around 1.05 dB cm^{-1} [46].

Since the average grain size is submillimeter ($\delta \approx 0.7\text{ mm}$) and the 3.5-MHz frequency results in a P -wave wavelength $\Lambda = 1.1\text{ mm}$, the ultrasonic wave propagation occurs in between the Rayleigh ($\Lambda > \delta$) and the stochastic ($\Lambda \approx \delta$) scattering regimes. This means that the coherent component of the wave field is stronger than the incoherent one. The latter is suppressed in the ultrasonic measurements because the aperture of the ultrasonic transducer is sufficiently wide to average out the incoherent field.

The suppression of the incoherent field becomes less effective when the scans are performed with the 5-MHz probe. The shorter wavelength ($\Lambda = 0.8\text{ mm}$) leads to increased attenuation, $\zeta = 2.35\text{ dB cm}^{-1}$, which weakens the coherent field. Moreover, the incoherent field becomes stronger since the scattering regime is now fully stochastic and the suppression by transducer averaging is less effective since its aperture is narrower. As a result, the amplitude scan shows the speckle pattern observed in Fig. 8(b).

B. Oblique incidence analysis

The high levels of amplitude and travel-time variations observed with columnar ice, make this grain structure unsuitable for quantitative ultrasonic testing. Therefore, this section focuses on equiaxed ice tested at 3.5 MHz, which is the frequency yielding the highest degree of homogeneity. In order to operate at higher frequency, finer ice powders should be used during IPCM to yield smaller grain size. Although these can be produced with spray freezing techniques [47], this would require the development of a special setup, which, at this time, is beyond the scope of this work.

Figure 9 shows B scans of selected oblique incidence experiments performed with aluminum plates, the scan line being parallel to the SDH. At normal incidence ($\alpha = 0^\circ$), the scan shows a strong FS reflection (square arrow) followed by a weaker SDH reflection (round harrow). The reflections from the threaded holes are also visible (star arrows). When the angle of incidence increases to 30° , the FS reflection vanishes due to specular reflection leaving only the reflections from the SDH and threaded holes. Similar features are observed at 60° and 75° ; the latter being the largest angle that could be tested with the

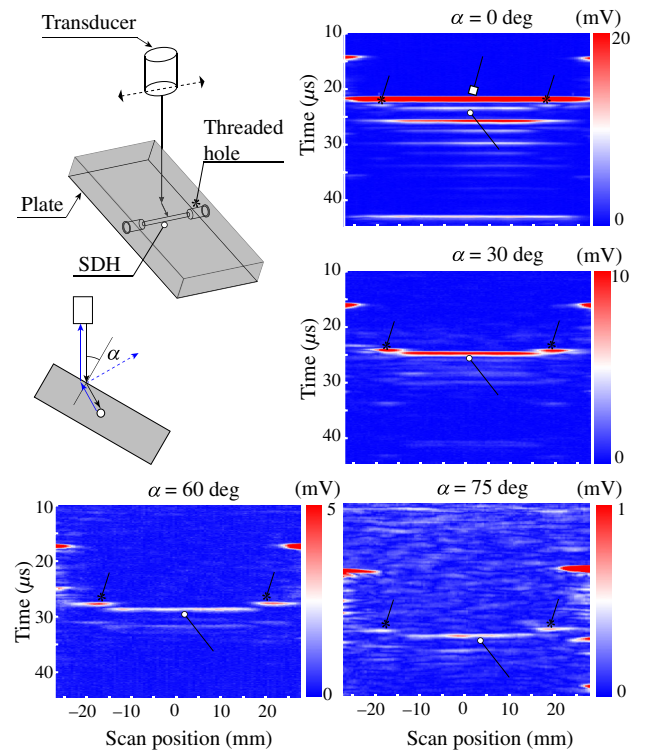


FIG. 9. B scans along a line parallel to the SDH for four different angles of incidence at 3.5 MHz. The specimen is an aluminum plate embedded in equiaxed ice. The round-head arrows indicate the SDH, the star arrows the threaded holes, and the square arrow the front-surface reflection that is only detectable at normal incidence ($\alpha = 0^\circ$).

current fixtures. It is remarkable that even at $\alpha = 75^\circ$, the reflection from the SDH is still clearly detectable. The background noise, which is more than 40 dB below the FS reflection amplitude (at normal incidence), is caused by weak backscattering at the grain boundaries, which results from a combination of grain anisotropy and the microbubbles that tend to accumulate at the grain boundaries.

The scattering mechanism that causes the SDH reflection at 60° and 75° is different from that involved at lower angles. This is shown in Fig. 10, which compares selected snapshots of FDTD simulations for a low (30°) and a high (60°) angle of incidence; animations of the full-wave propagation are available within the Supplemental Material [48]. The simulations are based on the effective properties of polycrystalline ice in Table I.

The structure of the field excited by the transducer can be observed at time $t = 5\ \mu\text{s}$. It consists of a plane wave propagating normal to the surface of the transducer and two pairs of cylindrical waves radiating from the two edges of the transducer aperture. They are referred to as edge waves and are of type P and S [49]. At 30° incidence, the field transmitted into the plate is the superposition of the

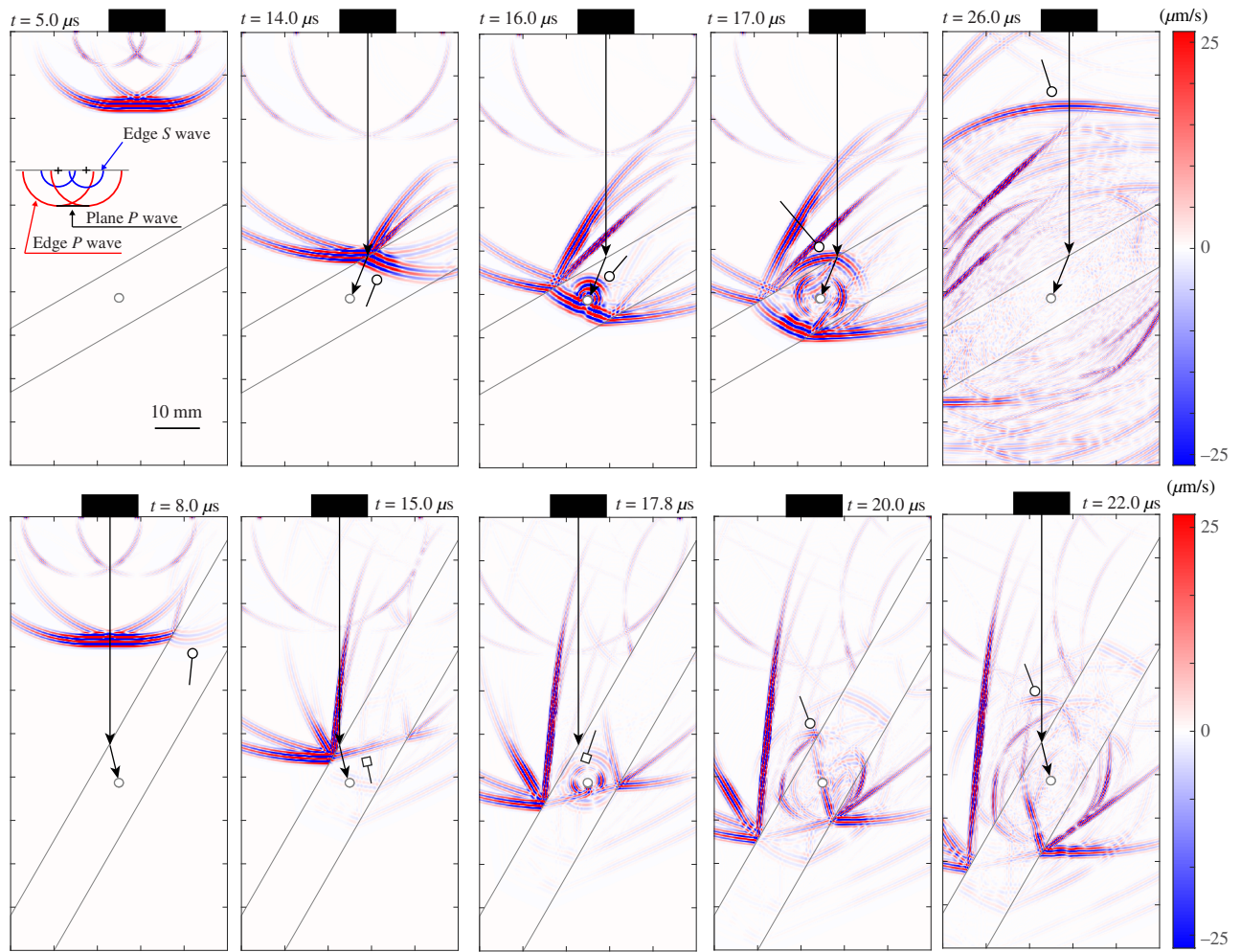


FIG. 10. FDTD simulations of the scattering of a 3.5-MHz ultrasonic beam by an aluminum plate embedded in ice at 30° (top row) and 60° (bottom row) incidence. The maps show the vertical component of the velocity field at selected time instances. The transducer and its widths are represented by the black rectangles. The arrow departing from the center of the transducer represents the ray path of an ideal plane wave. Round- and square-head arrows indicate the lead front of P and S waves, respectively.

refracted plane P wave (round arrow) and the weaker edge P wave as it can be seen from the snapshot at $t = 14 \mu\text{s}$, which also includes the ray path for an ideal plane wave. Once the refracted P wave reaches the SDH, it is scattered into a quasicylindrical P wave ($t = 16 \mu\text{s}$), which propagates toward the plate-ice interface where it experiences further refraction to generate an emerging P wave that advances toward the transducer ($t = 17 \mu\text{s}$, and $t = 26 \mu\text{s}$). At each of these steps, weaker S waves are also generated due to mode conversion.

At 60° incidence, the planar P wave experiences total reflection and only the edge P wave is transmitted inside the plate albeit with very low amplitude ($t = 8 \mu\text{s}$). On the other hand, a strong S wave is transmitted through the ice-plate interface as shown at $t = 15 \mu\text{s}$ (square arrow). The S wave is scattered by the SDH into both P and S waves ($t = 17.8 \mu\text{s}$). As the scattered S wave emerges from the plate, it is mode converted into a P wave ($t = 20 \mu\text{s}$), which then

propagates towards the transducer ($t = 22 \mu\text{s}$) to yield the SDH reflection.

For all cases, the travel time of the simulated SDH reflection matches the value predicted from ray theory and is also in agreement with the travel time measured experimentally. A comparison between FDTD simulations and experiments is provided in Fig. 11, which refers to the amplitude of the SDH reflection. The reflection coefficient, R , is defined as the ratio between the amplitude of the SDH reflection and the amplitude of the FS reflection at normal incidence. Experimentally, the SHD and the FS amplitudes are obtained from the C scans of the oblique and reference plate, respectively. The normalization of the SDH reflection makes the data independent of electronics settings and transducer electromechanical response and also removes the effect of attenuation in ice.

The good agreement between experiments and simulations further validates the hypothesis that equiaxed ice

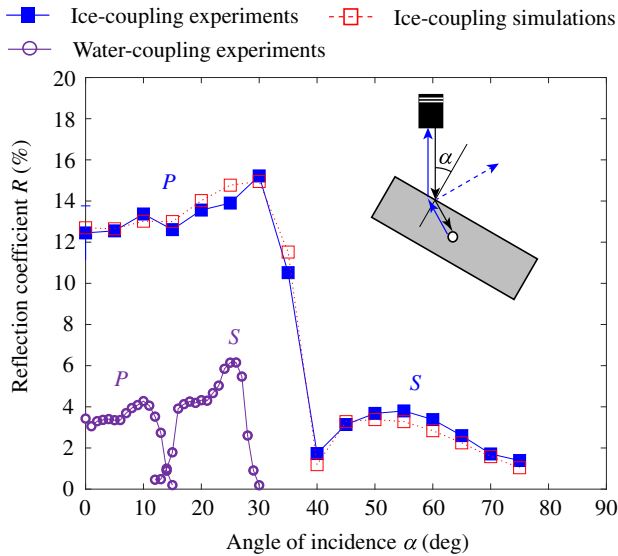


FIG. 11. Normalized reflection from a side-drilled hole in an aluminum plate as a function of angle of incidence, α , at 3.5 MHz. Experiments and simulations with equiaxed ice coupling (squares); experiments with water coupling (circles). Depending on α , the wave transmitted inside the plate and causing the reflection from the SDH can either be a compressional (P) or a shear (S) wave.

behaves as a homogeneous and isotropic material. Moreover, the trend of R as a function of α is consistent with the theoretical calculations of power transmission in Fig. 1 and confirms that ultrasonic transmission through an ice-aluminum interface can be achieved regardless of the orientation of the ultrasonic beam. This is thanks to the broader range of angles over which P waves can be transmitted (up to approximately 40°) and the presence of a mode converted S wave for all other higher angles. Conversely, immersion restricts testing to angles below 30° as shown by the experimental water coupling data also given in Fig. 11 [50].

The effectiveness of ice coupling is further demonstrated in Fig. 12, which provides the reflection coefficient measured at $\alpha = 30^\circ$ and $\alpha = 60^\circ$ for the four different metals listed in Table I. The data is plotted as a function of the impedance of P waves in each material ($Z = c_P^m \rho$) and for each experiment the corresponding result from the FDTD simulations is also given. The good agreement between experiments and simulations implies that the atomic composition of different metals does not affect the bond condition at the ice-metal interface. If weaker bonding occurred, this would result in lower transmission and hence cause the measured reflections to be substantially lower than the simulated one.

As expected, the reflection coefficient decreases as material impedance increases due to the higher contrast with the mechanical properties of ice. However, even for the worst-case scenario, which occurs with Inconel 718 at

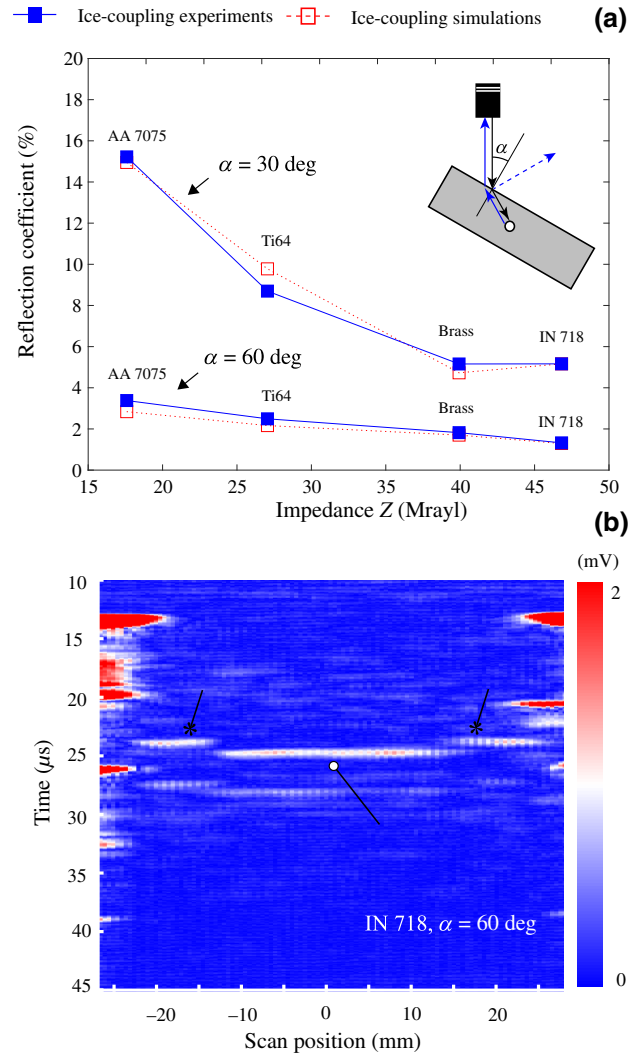


FIG. 12. (a) Performance of equiaxed ice coupling at 3.5 MHz for different metallic alloys. The normalized side-drilled hole reflection is shown as a function of the compressional wave impedance in each material for $\alpha = 30^\circ$ and $\alpha = 60^\circ$ incidence. The alloys considered are aluminum 7075 (AA 7075), titanium Ti-6Al-4V (Ti64), brass, and Inconel 718 (IN 718). Experiments (solid squares); simulations (open squares). (b) Experimental B scan of the SDH (round arrow) in the IN 718 plate at $\alpha = 60^\circ$ incidence.

$\alpha = 60^\circ$, the SHD is still clearly detectable as shown in the B scan of Fig. 12(b).

IV. CONSIDERATIONS ON PRACTICAL NONDESTRUCTIVE TESTING APPLICATIONS

The use of ice coupling for routine nondestructive inspections will, in general, require more demanding procedures compared to conventional immersion ultrasonic testing. In particular, specimen preparation and temperature control can add a degree of complexity to the inspection process. Therefore, ice coupling should be employed

when immersion ultrasonics cannot achieve sufficient sensitivity either due to the presence of highly curved geometries or components with internal features that would result in multiple water-metal interfaces. There are also some conventional testing configurations for which ice coupling can offer some benefits over immersion by avoiding the need for costly surface treatments, which may be required prior to immersion ultrasonic testing. For instance, under immersion, poor sensitivity is achieved through interfaces with high surface roughness because roughness causes phase modulation that reduces the coherence of the wave field transmitted through the interface and leads to significant signal attenuation. As a result, it is often necessary to machine the surface of a component before testing. The phase-modulation phenomenon is driven by the ultrasonic velocity contrast between water and metals and is greatly reduced when water is replaced by ice owing to its higher velocity. Preliminary experiments, similar to those presented in Fig. 12, have shown that relatively high surface roughness levels ($R_a \approx 20 \mu\text{m}$) have a negligible effect on the amplitude of the SDH reflection.

From a practical perspective, the main burden associated with specimen preparation is represented by the time required to freeze the ice volume. Very long freeze times can become impractical when the inspection is used for quality control at manufacture since it can affect the throughput of a production line. Similarly, during in-service inspections, only a limited time window is allowed to minimize asset downtime. As shown in Ref. [13], the freeze time increases with the square of the thickness of the ice volume (while it is independent of the volume width) and is inversely proportional to the temperature of the directional freezer (expressed in Celsius). As an example, with a freezer temperature of -15°C it takes approximately 13 h to freeze a 100-mm-thick volume of water. This time drops to 6.5 h if the freezer is operated at -30°C . A further reduction is achieved with ICPM since the freeze time is now proportional to the water-volume fraction. With high ice-particle compaction, the water-volume fraction can be reduced well below 0.5, thus cutting the freeze time by more than 50%. In the example above, this leads to a freeze time of less than 3.25 h. In this context, it should be emphasized that the ice powders used with ICPM are inexpensive and can be produced with a variety of methods ranging from crushing ice blocks in a blender, as it is done in this work, to using flash-freezing techniques [47].

Ultrasonic scans under ice coupling can be performed with the same ultrasonic equipment (electronics, transducers, computer-controlled scanners, etc.) used in conventional ultrasonic testing; this also ensures that scan times are the same. However, there is a need for additional custom-made items, including the directional freezer and a cold room or large freezer (maintained at around -10°C), which increase the equipment capital cost to some extent.

V. CONCLUSIONS

The effectiveness of ultrasonic testing with ice coupling is greatly improved when the solid under inspection is encapsulated in a block of ice, which has a fine, equiaxed polycrystalline structure in addition to being free from pores and cracks.

Applying directional freezing to a solid immersed in water alone can prevent pores and cracks but leads to a coarse columnar grain structure. This causes the ice volume to appear highly inhomogeneous when ultrasonic waves are propagated through the grains due to the anisotropy of ice Ih crystals. As a result, the interpretation of the ultrasonic signals is complicated by large amplitude and travel-time variations that correlate with the underlying grain structure and which can mask the signatures from reflectors of interest, e.g., flaws within the solid.

The columnar growth can be inhibited by compacting small ice particles around the solid and subsequently saturating them with degassed water before applying directional freezing. This technique produces an equiaxed structure and has also the advantage of reducing freezing time since the amount of liquid water is reduced by the volume fraction of the ice particles. When the grain size is sufficiently small compared to the ultrasonic wavelength, the effect of individual grains is averaged out leading to an effective medium that is homogeneous and isotropic. Therefore, ultrasonic waves propagate in the ice medium freely without distortion albeit with some degree of attenuation.

The equations of elastodynamics provide an accurate framework to simulate the complex wave interactions that occur at the ice-solid interfaces and within the solid itself. For a fine equiaxed grain structure, it is sufficient to model ice as an isotropic and homogenous medium defined by the effective properties of the polycrystalline material. The framework will therefore be useful to implement advanced imaging techniques such as seismic migration, which is particularly effective in media with sudden impedance changes similar to those observed at ice-metal interfaces.

Of note, oblique incidence experiments demonstrate that ultrasonic transmission through an ice-metal interface is possible regardless of the angle formed between the incident ultrasonic beam and the interface. This contrasts conventional immersion testing where the maximum angle of incidence is limited by the shear-wave critical angle above which total reflection occurs. Such a critical angle does not exist under ice coupling because the speed of compressional waves in ice is usually greater than the shear velocity in metals. Since high angles of incidence are unavoidable in the presence of solids with complex geometrical contours, ice coupling provides a promising approach to the ultrasonic inspection of highly complex engineering components and could therefore address a long-standing challenge in the field of nondestructive evaluation.

ACKNOWLEDGMENTS

This material is based on research sponsored by AFRL under Agreement No. FA8650-20-1-5201. The U.S. Government is authorized to reproduce and distribute reprints for Governmental purposes notwithstanding any copyright notation thereon.

-
- [1] D. Bonamy and K. Ravi-Chandar, Interaction of Shear Waves and Propagating Cracks, *Phys. Rev. Lett.* **91**, 235502 (2003).
- [2] J. Potter, A. Croxford, and P. Wilcox, Nonlinear Ultrasonic Phased Array Imaging, *Phys. Rev. Lett.* **113**, 144301 (2014).
- [3] G. Yan, S. Raetz, N. Chigarev, V. E. Gusev, and V. Tournat, Characterization of Progressive Fatigue Damage in Solid Plates by Laser Ultrasonic Monitoring of Zero-Group-Velocity Lamb Modes, *Phys. Rev. Appl.* **9**, 061001 (2018).
- [4] *Nondestructive Testing Handbook, Third Edition: Ultrasonic Testing*, edited by G. L. Workman, D. Kishoni, and P. O. Moore, Vol. 7 (American Society for Nondestructive Testing, Columbus, OH, 2007).
- [5] W. E. Frazier, Metal additive manufacturing: A review, *J. Mater. Eng. Perform.* **23**, 1917 (2014).
- [6] J. M. Waller, R. L. Saulsbury, B. H. Parker, K. L. Hodges, E. R. Burke, K. M. Taminger, D. E. Chimenti, and L. J. Bond, in *AIP Conference Proceedings*, Vol. 1650 (AIP, 2015), p. 51.
- [7] S. K. Everton, M. Hirsch, P. Stravroulakis, R. K. Leach, and A. T. Clare, Review of in-situ process monitoring and in-situ metrology for metal additive manufacturing, *Mater. Des.* **95**, 431 (2016).
- [8] M. Seifi, M. Gorelik, J. Waller, N. Hrabe, N. Shamsaei, S. Daniewicz, and J. J. Lewandowski, Progress towards metal additive manufacturing standardization to support qualification and certification, *Jom* **69**, 439 (2017).
- [9] E. L. Gromnitskaya, O. V. Stal'gorova, V. V. Brazhkin, and A. G. Lyapin, Ultrasonic study of the nonequilibrium pressure-temperature diagram of H₂O ice, *Phys. Rev. B* **64**, 094205 (2001).
- [10] V. F. Petrenko and R. W. Whitworth, *Physics of Ice* (Oxford University Press, Oxford, 1999).
- [11] T. Bartels-Rausch, V. Bergeron, J. Cartwright, R. Escribano, J. Finney, H. Grothe, P. J. Gutiérrez, J. Haapala, W. F. Kuhs, and J. B. C. Pettersson, *et al.*, Ice structures, patterns, and processes: A view across the icefields, *Rev. Mod. Phys.* **84**, 885 (2012).
- [12] F. Simonetti, I. L. Satow, A. J. Brath, K. C. Wells, J. Porter, B. Hayes, and K. Davis, Cryo-ultrasonic NDE: Ice-coupled ultrasonic waves for the detection of damage in complex-shaped engineering components, *IEEE Trans. Ultrason. Ferroelectr. Freq. Control* **65**, 638 (2018).
- [13] F. Simonetti and M. Fox, Experimental methods for ultrasonic testing of complex-shaped parts encased in ice, *NDT E Int.* **103**, 1 (2019).
- [14] W. Xu, M. Yuan, W. Xuan, X. Ji, and Y. Chen, Quantitative inspection of complex-shaped parts based on ice-coupled ultrasonic full waveform inversion technology, *Appl. Sci.* **11**, 4433 (2021).
- [15] J. Achenbach, *Wave Propagation in Elastic Solids*, Vol. 16 (Elsevier, Amsterdam, 2012).
- [16] L. E. Raraty and D. Tabor, The adhesion and strength properties of ice, *Proc. R. Soc. London. Ser. A, Math. Phys. Sci.*, 184 (1958).
- [17] P. Archer and V. Gupta, Measurement and control of ice adhesion to aluminum 6061 alloy, *J. Mech. Phys. Solids* **46**, 1745 (1998).
- [18] K. Matsumoto and T. Kobayashi, Fundamental study on adhesion of ice to cooling solid surface, *Int. J. Refrig.* **30**, 851 (2007).
- [19] M. Zou, S. Beckford, R. Wei, C. Ellis, G. Hatton, and M. Miller, Effects of surface roughness and energy on ice adhesion strength, *Appl. Surf. Sci.* **257**, 3786 (2011).
- [20] R. Li, A. Alizadeh, and W. Shang, Adhesion of liquid droplets to rough surfaces, *Phys. Rev. E* **82**, 041608 (2010).
- [21] D. vdS Roos, Rapid production of single crystals of ice, *J. Glaciol.* **14**, 325 (1975).
- [22] R. Abbasi, Y. Abdou, M. Ackermann, J. Adams, J. A. Aguilar, M. Ahlers, D. Altmann, K. Andeen, J. Auffenberg, X. Bai, and M. Baker, Ictop: The surface component of icecube, *Nucl. Instrum. Methods Phys. Res. Sect. A: Accelerators, Spectrometers, Detectors and Associated Equipment* **700**, 188 (2013).
- [23] J. Tamura, Y. Kogure, and Y. Hiki, Ultrasonic attenuation and dislocation damping in crystals of ice, *J. Phys. Soc. Jpn.* **55**, 3445 (1986).
- [24] B. R. Thompson, Elastic-wave propagation in random polycrystals: Fundamentals and application to nondestructive evaluation, Imaging of complex media with acoustic and seismic waves, 233 (2002).
- [25] R. L. Weaver, Diffusivity of ultrasound in polycrystals, *J. Mech. Phys. Solids* **38**, 55 (1990).
- [26] S. Hirsekorn, The scattering of ultrasonic waves by polycrystals, *J. Acoust. Soc. Am.* **72**, 1021 (1982).
- [27] F. E. Stanke and G. S. Kino, A unified theory for elastic wave propagation in polycrystalline materials, *J. Acoust. Soc. Am.* **75**, 665 (1984).
- [28] C. M. Kube and J. A. Turner, Ultrasonic attenuation in polycrystals using a self-consistent approach, *Wave Motion* **57**, 182 (2015).
- [29] A. P. Arguelles and J. A. Turner, Ultrasonic attenuation of polycrystalline materials with a distribution of grain sizes, *J. Acoust. Soc. Am.* **141**, 4347 (2017).
- [30] M. Ryzy, T. Grabec, P. Sedlák, and I. A. Veres, Influence of grain morphology on ultrasonic wave attenuation in polycrystalline media with statistically equiaxed grains, *J. Acoust. Soc. Am.* **143**, 219 (2018).
- [31] G. Sha, M. Huang, M. Lowe, and S. Rokhlin, Attenuation and velocity of elastic waves in polycrystals with generally anisotropic grains: Analytic and numerical modeling, *J. Acoust. Soc. Am.* **147**, 2442 (2020).
- [32] A. Maurel, F. Lund, and M. Montagnat, Propagation of elastic waves through textured polycrystals: Application to ice, *Proc. R. Soc. A: Math., Phys. Eng. Sci.* **471**, 20140988 (2015).
- [33] P. Camp, The formation of ice at water-solid interfaces, *Ann. N. Y. Acad. Sci.* **125**, 317 (1965).

- [34] E. Pach, L. Rodriguez, and A. Verdaguer, Substrate dependence of the freezing dynamics of supercooled water films: A high-speed optical microscope study, *J. Phys. Chem. B* **122**, 818 (2018).
- [35] A. J. Gow, Orientation textures in ice sheets of quietly frozen lakes, *J. Cryst. Growth* **74**, 247 (1986).
- [36] D. M. Cole, Preparation of polycrystalline ice specimens for laboratory experiments, *Cold Reg. Sci. Technol.* **1**, 153 (1979).
- [37] W. Durham, H. Heard, and S. H. Kirby, Experimental deformation of polycrystalline H₂O ice at high pressure and low temperature: Preliminary results, *J. Geophys. Res.: Solid Earth* **88**, B377 (1983).
- [38] P. Lehto, H. Remes, T. Saukkonen, H. Hänninen, and J. Romanoff, Influence of grain size distribution on the Hall–Petch relationship of welded structural steel, *Mater. Sci. Eng.: A* **592**, 28 (2014).
- [39] P. Moczo, J. O. Robertsson, and L. Eisner, The finite-difference time-domain method for modeling of seismic wave propagation, *Adv. Geophys.* **48**, 421 (2007).
- [40] J. Virieux, P-SV wave propagation in heterogeneous media: Velocity-stress finite-difference method, *Geophysics* **51**, 889 (1986).
- [41] R. W. Graves, Simulating seismic wave propagation in 3D elastic media using staggered-grid finite differences, *Bull. Seismol. Soc. Am.* **86**, 1091 (1996).
- [42] F. Collino and C. Tsogka, Application of the perfectly matched absorbing layer model to the linear elastodynamic problem in anisotropic heterogeneous media, *Geophysics* **66**, 294 (2001).
- [43] A. R. Levander, Fourth-order finite-difference P-SV seismograms, *Geophysics* **53**, 1425 (1988).
- [44] W. Zhang and X. Chen, Traction image method for irregular free surface boundaries in finite difference seismic wave simulation, *Geophys. J. Int.* **167**, 337 (2006).
- [45] J. Tatibouet, R. Vassoille, and J. Perez, Ultrasonic properties of plastically deformed ice, *J. Glaciol.* **15**, 161 (1975).
- [46] Attenuation measurements are notoriously difficult and a new setup is being built to improve measurement accuracy and also to determine the attenuation of *S* waves.
- [47] N. Azuma, T. Miyakoshi, S. Yokoyama, and M. Takata, Impeding effect of air bubbles on normal grain growth of ice, *J. Struct. Geol.* **42**, 184 (2012).
- [48] See Supplemental Material at <http://link.aps.org/supplemental/10.1103/PhysRevApplied.18.014034> for wave-propagation animations.
- [49] J. P. Weight, A model for the propagation of short pulses of ultrasound in a solid, *J. Acoust. Soc. Am.* **81**, 815 (1987).
- [50] The immersion measurements are performed by maintaining the exact same experimental parameters as in the ice tests, i.e., same transducer, fixtures, scanner, plates, etc.